Journal Pre-proofs

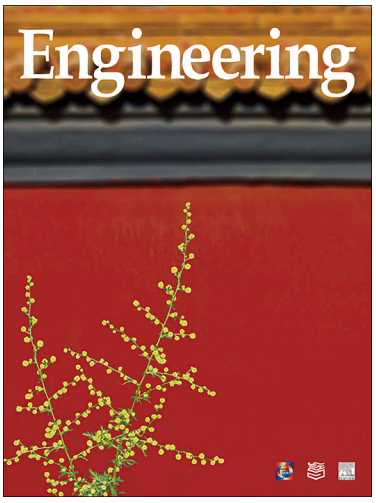


Article

# A Diamond-Lattice-Structure-Inspired Full-Polarized Lightweight Steady Isotropic Luneburg Lens

Yuechao Wang, Kai Chen, Jun Xu, Ka Fai Chan, Xiaoyue Xia, Sai Ma, Yiqiu Liang, Chi-Hou Chan, Wei Hong

PII: S2095-8099(25)00816-1
DOI: https://doi.org/10.1016/j.eng.2025.12.027
Reference: ENG 2202

To appear in: *Engineering*

Received Date: 10 April 2025
Revised Date: 2 November 2025
Accepted Date: 9 December 2025

Please cite this article as: Y. Wang, K. Chen, J. Xu, K.F. Chan, X. Xia, S. Ma, Y. Liang, C-H. Chan, W. Hong, A Diamond-Lattice-Structure-Inspired Full-Polarized Lightweight Steady Isotropic Luneburg Lens, *Engineering* (2026), doi: https://doi.org/10.1016/j.eng.2025.12.027

Advanced Antennas for Wireless Connectivity—Article

# A Diamond-Lattice-Structure-Inspired Full-Polarized Lightweight Steady Isotropic Luneburg Lens

Yuechao Wang [a,#], Kai Chen [a,#], Jun Xu [a,*], Ka Fai Chan [b], Xiaoyue Xia [b], Sai Ma [a], Yiqiu Liang [a], Chi-Hou Chan [b], Wei Hong [a,c,*]

[a] *State Key Laboratory of Millimeter Waves, School of Information Science and Engineering, Southeast University, Nanjing 210096, China*

[b] *State Key Laboratory of Terahertz and Millimeter Waves, City University of Hong Kong, Hong Kong 999077, China*

[c] *Purple Mountain Laboratories, Nanjing 211111, China*

[#] These authors contributed equally to this work.

* Corresponding authors.

*E-mail addresses:* junxu@seu.edu.cn (J. Xu), weihong@seu.edu.cn (W. Hong).

**ABSTRACT**

This article presents a novel, lightweight, full-polarized Luneburg lens (LL) antenna featuring a diamond lattice structure for the first time. While retaining the essential attributes of a full-scale LL, such as pencil-beam generation capability, high gain, wide bandwidth, and omnidirectional scanning, this LL leverages the isotropic nature of its diamond crystal structure to seamlessly adapt to various polarizations and a wide range of incident wave angles. Utilizing advanced three-dimensional-printing (3DP) technology, an intricately designed structure was fabricated. An elaborate wideband feeding system was also developed to serve as the primary feed for the lens. The proposed system supports typical polarization states and consists of a dual-polarized horn antenna integrated with a sextuple-polarized feeding network. The results indicate that the operation bandwidth of the proposed LL antenna covers the entire X-band (8–12 GHz) under any polarization scenario. Furthermore, the antenna exhibits consistent and stable gains, thereby simplifying the design complexity of signal processing systems. Compared with conventional LLs constructed with a cubic lattice structure, this innovative LL antenna boasts a reduced weight and diminished sidelobe levels. These advancements position the proposed design as a promising candidate for satellite communications, integrated sensing and communication, microwave imaging, and diverse future endeavors.

**KEYWORDS**

Luneburg lens

Diamond lattice structure

Three-dimensional-printed antenna

Multibeam antenna

## 1. Introduction

Multibeam antennas are indispensable devices across diverse domains, such as wireless communication, radar systems, and microwave imaging, and consistently surpass performance expectations [1–4]. Such antennas are required to exhibit exceptional characteristics, including high gain, excellent isolation, negligible sidelobe, broad operational bandwidth, and versatile multi-polarization capabilities, to streamline signal processing systems and reduce costs. As an alternative to their active counterparts, passive multibeam antennas leveraging lenses for beamforming have sparked significant research interest, owing to their cost-effective manufacturing processes and lower energy consumption.

Typically, lenses are classified into homogeneous dielectric lenses and gradient-index (GRIN) lenses [5]. The Luneburg lens (LL), a GRIN lens based on geometrical optics, effectively converts incoming spherical waves into outgoing plane waves and vice versa, while maintaining a constant aperture across a wide range of incident angles. This lens offers a viable approach for achieving precise wide-angle beam control with low cross-polarization discriminations [6]. Nevertheless, the realization of an ideal LL is currently impeded by the absence of suitable materials, due to the requirement that the refractive index $n$ must follow a radial distribution [7]:

$n(R) = \sqrt{2 - R^2}$ (1)

where $R$ is the normalized radius. Therefore, traditional LLs are crafted using a series of concentric shells that approximates the theoretical permittivity curve in a stepped manner. This manufacturing process poses significant challenges stemming from the stringent demands for shape accuracy and interlayer permittivity precision [8–10]. Although various two-dimensional (2D) designs—such as printed circuit board (PCB)-stacked LL antennas [11–13], columnar LL antennas [14–16], and parallel-plate waveguide/dielectric slab configurations [17–19]—reduce the overall profile and processing difficulty, they encounter limitations in achieving narrow beamwidths and wide scanning angles simultaneously across both the plane parallel to the direction of the electric field (E-plane ) and the plane parallel to the direction of the magnetic field (H-plane ). Therefore, wide-angle beam scanning in both the elevation and azimuth planes remains elusive [20]. Nevertheless, in complex scenarios demanding robust and high-capacity data transmission across various directions, such as in satellite communications, full-scale LLs have unmatched advantages [21]. Based on the effective medium theory (EMT), three-dimensional-printing (3DP) technology has facilitated the cost-effective implementation of GRIN materials by filling periodic unit cells with precalculated volumes of materials. This advancement has enabled the production of LLs with expansive operational bandwidths and simplified processing methods.

In communication systems, isotropic antennas—which exhibit radiation characteristics independent of excitation polarization and direction—can achieve wide-angle steering while simplifying signal processing systems [22]. A variety of unit structures have been employed in three-dimensional (3D)-printed full-scale LL designs, including dielectric holes [5,23,24], cubic lattices [25,26], dielectric slabs [27], rod configurations [7,28–30], and curved elements [31]. The asymmetry present in dielectric holes [23,24], dielectric slabs [27], and rod configurations [28,29] across different directions results in an effective permittivity that varies with the angle of incidence or polarization states, making these LLs unsuitable for the simultaneous provision of a stable linearly polarized and circularly polarized performance [28]. Furthermore, the bandwidth and radiation characteristics of the feed directly influence the performance of LL antennas. To the best of our knowledge, no report has validated the concurrent performance of linearly polarized and circularly polarized radiation. Therefore, the design of a full-polarized LL antenna holds significant importance.

Compact lightweight antennas are the primary goal of modern wireless communication and sensing systems. Table 1 summarizes the spatial occupancy rate of common crystal structures [32]. While a 3D-printed LL with a cubic lattice structure exhibits satisfactory isotropic performance [26], its simple cubic packing structure results in a spatial occupancy rate of 52%, imparting substantial weight to the LL. Conversely, in the unit cell of a diamond crystal structure, each atom is surrounded by four atoms, forming a 3D spatial structure through tetrahedral covalent bonding. This arrangement not only offers excellent isotropic performance but also boasts a space packing efficiency of just 34%, conferring substantial weight-reduction benefits.

**Table 1**

Spatial occupancy rate of common crystal cell structures.

| Type | Schematic diagram | Crystal length ($a_c$) versus atomic radius ($r$) | Atomic number | Spatial occupancy rate |
|---|---|---|---|---|
| Diamond cubic packing | 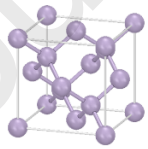 | $a_c = 8r/\sqrt{3}$ | 8 | 34% |
| Simple cubic packing | 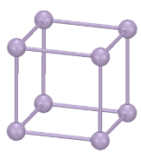 | $a_c = 2r$ | 1 | 52% |
| Body-centered cubic packing | 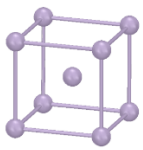 | $a_c = 4r/\sqrt{3}$ | 2 | 68% |

| | | | | |
|---|---|---|---|---|
| Hexa packing | 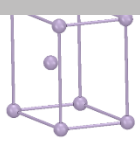 | | | |
| Face-centered cubic packing | 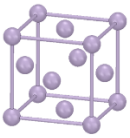 | $a_c = 2\sqrt{2}\,r$ | 4 | 74% |

This article introduces for the first time a novel diamond-lattice-structure-inspired lightweight LL that incorporates full polarizations—that is, horizontal linear polarization (H-LP), vertical linear polarization (V-LP), ±45° linear polarization (±45° LP), left-hand circular polarization (LHCP), right-hand circular polarization (RHCP), and so forth. The proposed design retains numerous advantages of traditional full-scale LLs, including the ability to generate a pencil beam, high gain, wide bandwidth coverage, and omnidirectional scanning capabilities. By leveraging the isotropy of its diamond crystal structure, the proposed LL can accommodate variations in arbitrary polarization states and incident wave angles. A wideband feeding system with six general polarizations is developed as the primary feed of the LL, consisting of a dual-polarized horn antenna and a sextuple-polarized feeding network. The experimental results demonstrate that, regardless of the polarization scenario, the operational bandwidth of the proposed antenna covers the entire X-band while maintaining consistent and smooth gains. This simplifies the design complexity of signal processing systems. Furthermore, the proposed LL showcases lower sidelobe levels, reduced weight, and simplified fabrication compared with conventional LLs constructed with a cubic lattice structure. As shown in Fig. 1, thanks to its exceptional characteristics of lightness, high gain, flexible beam steering, and polarization-switching capabilities, the proposed design holds significant potential for a wide array of advanced applications, including satellite communications, radar sensing, wireless power transfer, and microwave imaging. The integrated single-lens system with multiple feed sources achieves functional isolation through spatial separation and polarization orthogonality to prevent mutual interference. These distinctive features facilitate superior signal transmission efficiency, accurate target detection, effective energy delivery, and high-resolution imaging, thereby establishing the system as a highly versatile and robust solution for diverse applications in contemporary electromagnetic systems. Moreover, this work introduces a crystallography-inspired design strategy that facilitates the comprehensive and integrated optimization of electromagnetic components. By concurrently considering structural, material, and wave-related properties, this approach drives forward the progress of wireless communication technology and strengthens the connection between the realms of materials science and electromagnetic engineering.

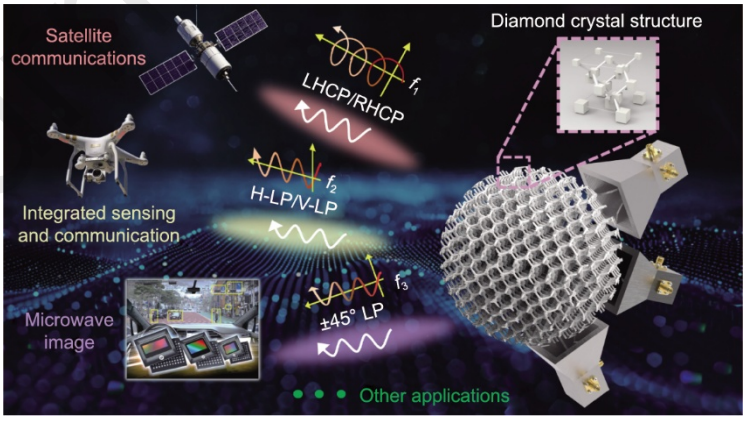


**Fig. 1.** Application of the proposed full-polarized multibeam LL antenna based on a diamond lattice structure. $f_1$, $f_2$, and $f_3$: multiple operational frequency bands of the proposed lens.

The remainder of this article proceeds as follows: Section 2 presents a detailed description of the proposed LL, encompassing its operating mechanism and design methodology. Section 3 focuses on the design and analysis of the sextuple-polarized feeding system. The simulated and measured results of the proposed LL antenna are detailed in Section 4. Section 5 provides a discussion, while a concise conclusion is presented in Section 6.

*2.1. Realization of varying permittivity*

Given the varying relative permittivity demands for a spherical LL ranging from 2 to 1, the material of choice was the photopolymer VeroClear, which boasts a permittivity of 2.9 and a loss tangent of 0.01 [15]. The model was simulated using the periodic boundaries in a full-wave electromagnetic simulator (High Frequency Structure Simulator, Ansys, USA). Due to constraints in computer memory, a prismatic configuration was favored over a curved surface structure to reduce the complexities of mesh generation. Fig. 2 illustrates the unit cell of the diamond crystal structure, which comprises four hexagonal prisms characterized by angles of arccos(–1/3) and a cube with variable side lengths. Limited by the minimum accuracy of 3DP technology, the basal side length of the hexagonal prism $l_m$ was specified at 0.75 mm to meet the minimal effective permittivity for the LL design. Subsequently, the effective permittivity of the unit cell was extracted using the *S*-parameter retrieval method [33], and the effective refractive index $n_e$ of the unit cell was modeled and computed by means of Eq. (2):

$$n_e = \frac{1}{|\boldsymbol{k}|a}\cos^{-1}\left[\frac{1}{2S}(1-S_{11}^2+S_{21}^2)\right] \qquad (2)$$

where $|\boldsymbol{k}|$ is the wavenumber of the electromagnetic wave; $a$ is the side length of the unit cell, which is 7.5 mm (less than half of the free-space wavelength) to mitigate any potential phase ambiguity [34]. Therefore, the equivalent permittivity $\varepsilon_e = n_e^2$ of the unit structure can be determined. The effective permittivity of the unit cell with different polymer cube sizes $w_c$, depicted in Fig. 2, harmonizes perfectly with the requirements of the lens design.

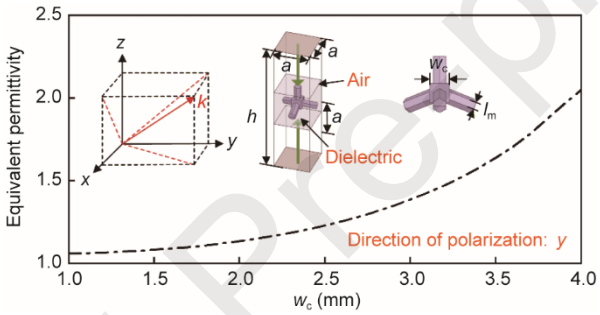


**Fig. 2.** Equivalent permittivity as a function of different polymer cube sizes $w_c$, with the cell of the diamond crystal structure included as an inset. $h$: the total height of the periodic boundary; $\boldsymbol{k}$: wave vector; $x$, $y$, and $z$: the three coordinate axes in the rectangular coordinate system.

To demonstrate the isotropy of the proposed crystal lattice structure, the unit cell is rotated around the *x*-, *y*-, and *z*-axes to explore the variation of the effective permittivity at different incident angles. Without loss of generality, Fig. 3 illustrates that the effective permittivity remains relatively constant within the range of 8–16 GHz for the cell configurations at rotation angles ($\alpha = 0°$, $\gamma = 0°$), ($\beta = 30°$, $\gamma = 0°$), and ($\alpha = 0°$, $\beta = 60°$), where $\alpha$, $\beta$, and $\gamma$ refer to the rotation angles of the cell around the $x$, $y$, and $z$ axes, respectively. A comparison between our diamond lattice structure and various classical structures—including post [28], cubic lattice [26], and body-centered cubic (BCC) lattice [35]—along with results is illustrated in Table 2 and Fig. 4, revealing that our lens exhibits more stable equivalent permittivity across different incidence angles and a lower variance in permittivity than its counterparts.

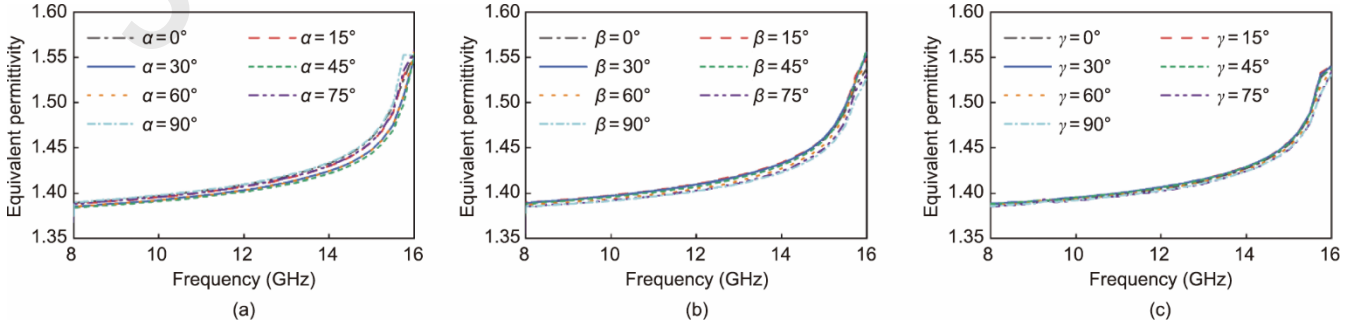


**Fig. 3.** Equivalent permittivity of the unit cell of a diamond crystal structure with different rotation angles of incidence: (a) $\beta = 30°$, $\gamma = 0°$, (b) $\alpha = 0°$, $\gamma = 0°$, and (c) $\alpha = 0°$, $\beta = 60°$.

**Table 2**

Comparison of our proposed diamond crystal unit cell with several classical unit cell configurations.



| Classification | Description | Crystal schematic diagram | Variance of $\varepsilon_e$ |
|---|---|---|---|
| Type A | Diamond lattice | 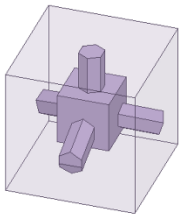 | $9.88\times10^{-6}$ |
| Type B | Post | 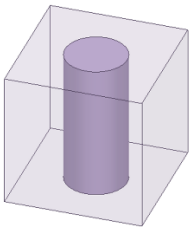 | $6.86\times10^{-4}$ |
| Type C | Simple cubic lattice | 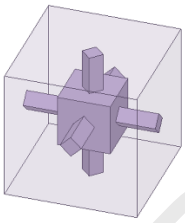 | $1.40\times10^{-5}$ |
| Type D | Body-centered cubic lattice | 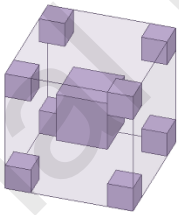 | $2.77\times10^{-3}$ |

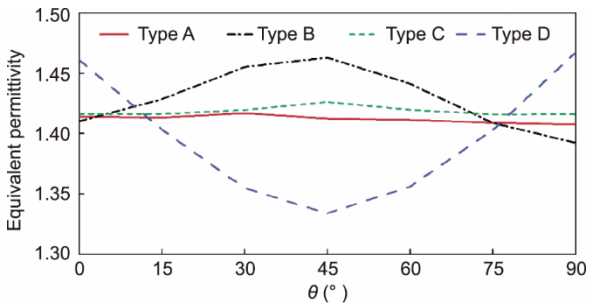


**Fig. 4.** Equivalent permittivity of different unit cells as a function of incident angle $\theta$.

*2.2 Discretization of the lens*

Compared with common LLs achieved through unit cell translation duplication, the proposed diamond-lattice-structure-inspired LL exhibits a more compact structure. The diamond lattice structure serves as the smallest repeating unit that encapsulates all symmetries of the crystal structure. Given the symmetry properties of the proposed LL, it is sufficient to consider merely one eighth of a sphere in order to attain the complete spherical configuration.

Moreover, the enhanced level of discretization of the LL sphere, characterized by an increasing number of stepwise gradient square units, results in a closer approximation to the ideal LL. However, as the quantity of discretized small units grows, there is a corresponding increase in the size of the LL sphere due to the fixed dimensions of each unit. As a result, the performance improvements gained from this increased discretization begin to diminish in returns. To strike a balance between the performance and size of the lens, as depicted in Fig. 5(b), the cell is translated fourfold along the *x*-, *y*-, and *z*-axes to configure one eighth of the overall structure, which is subsequently divided into ten layers, as shown in Fig. 5(c). By calculating the distance from the unit cell to the lens center, the side length of the cube—corresponding to the equivalent permittivity $\varepsilon_e$—is determined, as outlined in Table 3. To ensure the electromagnetic waves gather from all incident directions, the one-eighth structure is triplicated through mirroring, resulting in a spherical lens with a diameter of 147.8 mm, as depicted in Fig. 5(d).

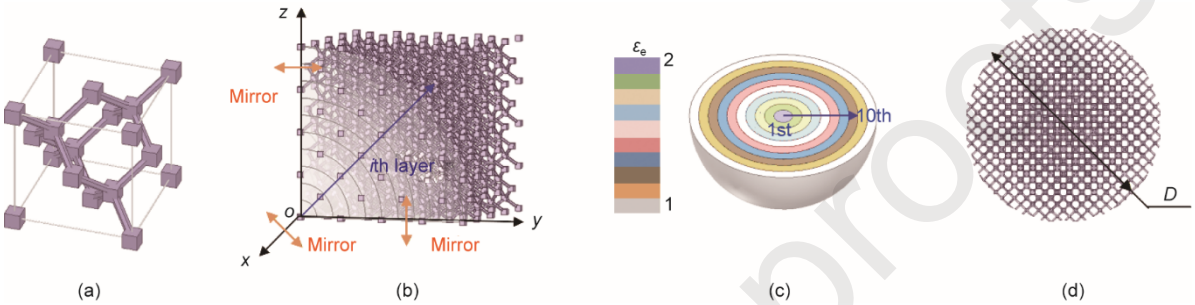


**Fig. 5.** Formation process of the proposed diamond-lattice-structure-inspired LL. (a) Crystal cell of the diamond structure; (b) an eighth of a cubic structure and ten layers; (c) schematic diagram of the LL discretization; (d) front view of the proposed LL design. *i*: the layer number determined based on the distance from the center of the lens, $i = 1, 2, \ldots, 10$; *o*: the center of the lens; *D*: diameter of the proposed lens.

**Table 3**

Polymer cube sizes $w_c$ at different layers constructing the proposed LL.

| *i*th layer | $\varepsilon_e$ | $w_c$ (mm) |
|---|---|---|
| 1 | 2.0 | 6.36 |
| 2 | 1.9 | 6.22 |
| 3 | 1.8 | 5.98 |
| 4 | 1.7 | 5.72 |
| 5 | 1.6 | 5.44 |
| 6 | 1.5 | 5.12 |
| 7 | 1.4 | 4.76 |

| | | |
|---|---|---|
| 8 | [illegible] | [illegible] |
| 9 | 1.2 | 3.64 |
| 10 | 1.1 | 2.44 |

## 3. Design of the feeding system

To ascertain the electromagnetic wave-gathering capability of the LL across multiple polarizations within the X-band at a lower cost, without loss of generality, Fig. 6(a) presents a schematic diagram of the wideband sextuple-polarized feeding system. This setup consists of a wideband dual-polarized horn antenna and a wideband sextuple-polarized feeding network. The feeding network encompasses various components, including a Wilkinson power divider (WPD), a 90° wideband phase shifter, and a 180° wideband phase shifter. Through strategic channel manipulation within the network, six distinct polarizations are attained for the horn antenna, as shown in Fig. 6(b). A comprehensive analysis of the design principles and detailed measured results is provided below.

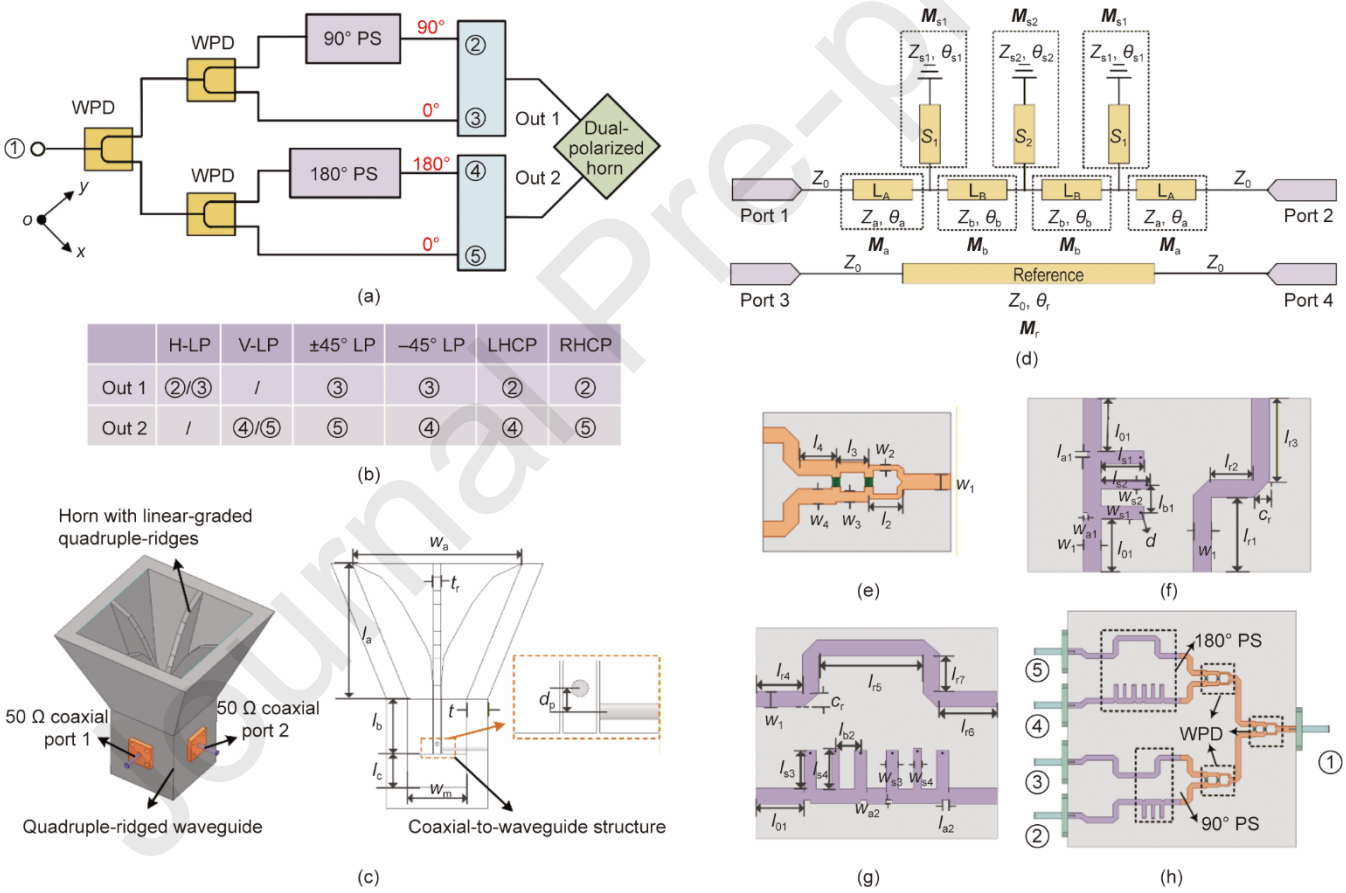


| | H-LP | V-LP | ±45° LP | –45° LP | LHCP | RHCP |
|---|---|---|---|---|---|---|
| Out 1 | ②/③ | / | ③ | ③ | ② | ② |
| Out 2 | / | ④/⑤ | ⑤ | ④ | ④ | ⑤ |

**Fig. 6.** (a) Schematic diagram of a wideband sextuple-polarized feeding system. (b) Feeding method for forming six polarizations. (c) Perspective view of the proposed dual-polarized quad-ridged horn antenna. $w_a = 46$ mm, $t_r = 2$ mm, $t = 6.2$ mm, $l_a = 41$ mm, $l_b = 17$ mm, $l_c = 9.5$ mm, $w_m = 16$ mm, and $d_p = 0.6$ mm. (d) Circuit configuration of the proposed 90° broadband phase shifter (PS); the proposed sextuple-polarized feeding network. $Z_0 = 50$ Ω. (e) Total model. (f) Wideband Wilkinson power divider (WPD). $w_1 = 1.66$ mm, $w_2 = 0.555$ mm, $l_2 = 3.75$ mm, $w_3 = 1.1$ mm, $l_3 = 3.5$ mm, $w_4 = 1.66$ mm, and $l_4 = 4$ mm. (g) 90° wideband PS. $l_{01} = 5$ mm, $l_{a1} = 0.55$ mm, $w_{a1} = 0.38$ mm, $l_{b1} = 2.6$ mm, $l_{s1} = 4$ mm, $w_{s1} = 1.275$ mm, $l_{s2} = 4.25$ mm, $w_{s2} = 0.85$ mm, $d = 0.2$ mm, $l_{r1} = 6$ mm, $l_{r2} = 3.89$ mm, $l_{r3} = 5.45$ mm, and $c_r = 1.45$ mm. (h) 180° wideband PS. $l_{a2} = 0.55$ mm, $w_{a2} = 0.42$ mm, $l_{b2} = 2.6$ mm, $l_{s3} = 4$ mm, $w_{s3} = 1.275$ mm, $l_{s4} = 4.25$ mm, $w_{s4} = 0.85$ mm, $l_{r4} = 4.64$ mm, $l_{r5} = 10.64$ mm, $l_{r6} = 6$ mm, and $l_{r7} = 3.68$ mm. $w_a$: aperture length of the horn; $t_r$: thickness of the ridge; $t$: thickness of the outer wall of the horn antenna; $l_a$: height of the horn section; $l_b$: height of the square waveguide; $l_c$: height of the matching block; $w_m$: width of the matching block and square waveguide; $d_p$: width of the matching block and waveguide; $\boldsymbol{M}_a$ and $\boldsymbol{M}_b$: the *ABCD* matrices of the transmission lines $L_A$ and $L_B$, respectively; $\boldsymbol{M}_{s1}$ and $\boldsymbol{M}_{s2}$: the *ABCD* matrices of the shorted stubs $S_1$ and $S_2$, respectively; $\boldsymbol{M}_r$**:** the *ABCD* matrices of the reference line, $Z_0$: characteristic impedance of the transmission lines; $\theta_{s1}$ and $\theta_{s2}$: the electrical lengths of shorted stubs $S_1$ and $S_2$, respectively; $\theta_a$, $\theta_b$, and $\theta_r$: the electrical lengths of transmission lines $L_A$ and $L_B$, and the reference line, respectively,; $Z_{s1}$ and $Z_{s2}$: the impedance of the electrical lengths of shorted stubs $S_1$ and $S_2$, repsectively; $Z_a$: the impedance of the electrical

lengths of transmission line $L_A$; $w_1$: width of the 50 Ω transmission line; $w_2$ and $l_2$: width and length of the first section of the power divider, respe[illegible] line after power division, respectively; $l_{01}$: length of the 50 Ω transmission line; $l_{a1}$ and $w_{a1}$: length and width of the notch of the 90° PS, respectively; $l_{b1}$ : length of transmission line *B* of the 90° PS; $l_{s1}$ and $w_{s1}$: length and width of the shorted stub $S_1$ of the 90° PS; $l_{s2}$ and $w_{s2}$ : length and width of shorted stub $S_2$ of the 90° PS, respectively; *d*: diameter of the shorting posts; $l_{r1}$ , $l_{r2}$, and $l_{r3}$: lengths of each part of the reference transmission line corresponding to the 90° PS; $c_r$: length of the bevel; $l_{a2}$ and $w_{a2}$: length and width of the notch of the 180° PS, respectively; $l_{b2}$: length of transmission line $L_B$ of the 180° PS; $l_{s3}$ and $w_{s3}$: length and width of the shorted stub $S_1$ of the 180° PS, respectively; $l_{s4}$ and $w_{s4}$: length and width of the shorted stub $S_2$ of the 180° PS, respectively; $l_{r4}$ , $l_{r5}$ , $l_{r6}$, and $l_{r7}$ : lengths of each part of the reference transmission line corresponding to the 180° PS.



### *3.1. Horn antenna*

A dual-polarized quadruple-ridged horn antenna is designed to serve as the feeding source of the proposed LL, providing wideband operation and multiple polarized incident waves. As depicted in Fig. 6(c), the horn antenna can be segmented into three parts: a quadruple-ridged waveguide, the horn with linear-graded quadruple-ridges, and a coaxial-to-waveguide structure. The overall length of the horn is set to 73.7 mm, with an aperture size width of 46 mm. Acknowledging the constraints imposed by the computer numerical control (CNC) milling machine on intricate structures [36], the designed horn antenna was fabricated using aluminum alloy 3DP technology and covers an operating frequency range of 7.8–13.8 GHz ($|S_{11}| < -10$ dB).

### *3.2. Feeding network*

Compared with traditional T-junction power dividers, the WPD has a distinct advantage in terms of impedance matching and high isolation at the output ports, which can reduce the crosstalk between output signals [37]. Based on the theory that the bandwidth of a power divider can be enhanced by employing multi-section transmission lines [38], a two-section WPD was detailed on a Rogers 4350 substrate, with a relative permittivity $\varepsilon_r$ of 2.2, a loss tangent tan$\delta$ of 0.0009, and a thickness $h_t$ of 0.76 mm.

A basic phase shifter is composed of two sections of transmission lines with different lengths—a configuration that only guarantees the necessary phase difference within a limited frequency range [39]. As shown in Fig. 6(d), the circuit configuration of the proposed 90° phase shifter was established by loading shorted stubs to expand the operational bandwidths, which can be analyzed using the *ABCD* matrix approach, as follows.

The electrical lengths $\theta_x$ of the shorted stubs $S_1$ and $S_2$, transmission lines $L_A$ and $L_B$, and reference line at operating frequency $f$ , can be defined as follows:

$$\theta_x = \theta_{x0}\frac{f}{f_0} \tag{3}$$

where $\theta_{x0}$ is the corresponding electrical length at center frequency $f_0$.

The *ABCD* matrices of the transmission lines ($\boldsymbol{M}_t$) and shorted lines ($\boldsymbol{M}_s$) can be written as follows [40]:

$$\boldsymbol{M}_t = \begin{bmatrix} \cos\theta_t & jZ_t\sin\theta_t \\ jY_t\sin\theta_t & \cos\theta_t \end{bmatrix} \tag{4}$$

$$\boldsymbol{M}_s = \begin{bmatrix} 1 & 0 \\ -jY_s\cot\theta_s & 1 \end{bmatrix} \tag{5}$$

where j is the imaginary part; $Z_t$ ,$Y_t$, and $\theta_t$ are the characteristic impedance, characteristic admittance, and electrical length of the transmission lines and reference line, respectively; $Y_s$ and $\theta_s$ are the characteristic admittance and electrical length of the shorted stubs, respectively. Therefore, the *ABCD* matrices of the main line and reference line shown in Fig. 6(d) can be deduced as follows:

$$\boldsymbol{M}_m = \boldsymbol{M}_a\boldsymbol{M}_{s1}\boldsymbol{M}_b\boldsymbol{M}_{s2}\boldsymbol{M}_b\boldsymbol{M}_{s1}\boldsymbol{M}_a = \begin{bmatrix} A_m & B_m \\ C & D \end{bmatrix} \tag{6}$$

$$\boldsymbol{M}_r = \begin{bmatrix} A_r & B_r \\ C & D \end{bmatrix} \tag{7}$$

where $\boldsymbol{M}_{\rm m}$ and $\boldsymbol{M}_{\rm r}$ are the $ABCD$ matrices of the main line and reference line, respectively; $\boldsymbol{M}_{\rm t}$ and $\boldsymbol{M}_{\rm L}$ are the $ABCD$ matrices of t[Journal Pre-proofs] $S_2$, respectively. To streamline the design and reduce complexity, the impedance $Z_{\rm b}$ is set to characteristic impedance $Z_0 = 50\ \Omega$. $A_{\rm m}$, $B_{\rm m}$, $C_{\rm m}$, and $D_{\rm m}$ are the voltage transfer ratio, transfer impedance, transfer admittance, and current rransfer ratio of the main line, respectively; $A_{\rm r}$, $B_{\rm r}$, $C_{\rm r}$, and $D_{\rm r}$ are the voltage transfer ratio, transfer impedance, transfer admittance, and current rransfer ratio of the reference line, respectively.

The insertion phase shift of the main line ($\Phi_{\rm m}$) and the reference line ($\Phi_{\rm r}$) can be derived as follows [39]:

$$\Phi_{\rm m}(f) = \angle S_{21}(f) = -\arctan\frac{B_{\rm m}/Z_0 + C_{\rm m}Z_0}{{\rm j}\left(A_{\rm m} + D_{\rm m}\right)} \tag{8}$$

$$\Phi_{\rm r}(f) = \angle S_{43}(f) = -\arctan\frac{B_{\rm r}/Z_0 + C_{\rm r}Z_0}{{\rm j}\left(A_{\rm r} + D_{\rm r}\right)} \tag{9}$$

The differential phase shift is attributed to the transmission phase disparity between the main line and the reference line. To keep the phase shift value $\Delta\varphi = 90°$ in the passband, the slopes of the phase shift need to be equal to zero; that is,

$$\Delta\varphi = \Phi_{\rm m}(f) - \Phi_{\rm r}(f) = 90^\circ \tag{10}$$

$$\frac{{\rm d}\Delta\varphi}{{\rm d}f} = 0 \tag{11}$$

Based on the provided design analysis, an iterative method was implemented in MATLAB (The MathWorks Inc., USA). The substrate chosen for this device was consistent with a WPD, as shown in Fig. 6(e). Design flexibility and size reduction can be achieved using curved reference lines. By connecting two 90° phase shifters (Fig. 6(f)) in series and appropriately adjusting the size of the lines, a 180° phase shifter was also developed, as depicted in Fig. 6(g). Further optimizations with a WPD were performed, and a sextuple-polarized feeding network was designed, as shown in Fig. 6(h); it was then fabricated through standard PCB processing. Employing a vector network analyzer (Keysight N5225B, Keysight Technologies, USA), the amplitude and phase responses of the fabricated sextuple-polarized feeding network were measured and are delineated in Fig. 7, exhibiting a notable concordance with the simulated results. It can be observed that the measured reflection coefficient is below −12 dB within the required frequency range of 8–12 GHz. The phase difference is equal to a specific phase shift with a ripple of less than ±6°, while the amplitude difference is less than 1 dB. These results provide the basis for the demonstration of a full-polarized LL antenna.

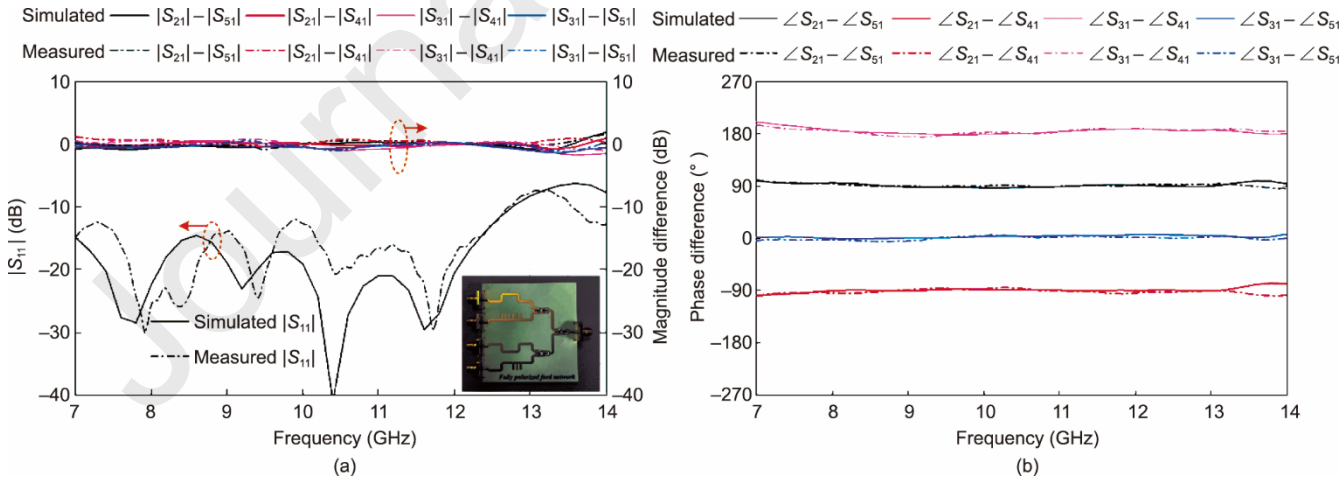


**Fig. 7.** Simulated and measured results of the proposed sextuple-polarized feeding network: (a) reflection coefficient and magnitude difference and (b) phase difference.

## 4. Simulated and experimental results

The dual-polarized horn antenna, introduced in Section 3, serves as the primary feeding source for the LL devised in Section 2. Fig. 8 illustrates the normalized radiation patterns and electric field distributions, both with and without the lens. The transformation of the spherical waves emitted by the horn feed into plane waves after passing through the lens, as

observed in both the E- and H-planes, validates the effectiveness of the proposed design methodology inspired by a diamond-latti



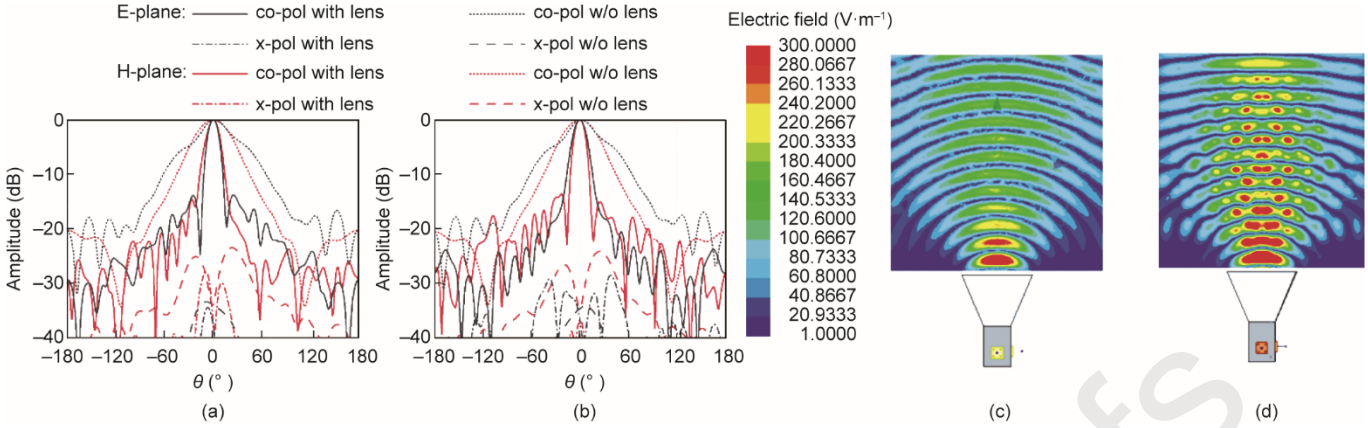


**Fig. 8.** Simulated normalized radiation patterns of the dual-polarized horn feed with and without the proposed LL at 10 GHz: (a) H-LP and (b) V-LP. Simulated electric field distributions of the dual-polarized horn feed excited by port 1 at 10 GHz (c) without lens and (d) with lens. Co-pol: co-polarization; x-pol: cross-polarization; w/o: without.

The LL antenna and its corresponding support were fabricated using 3DP technology. In order to meet the manufacturing requirements, the diameter of the lens was adjusted to 138 mm—a modification that was verified to have minimal impact on performance. Fig. 9(a) presents the simulated and measured *S*-parameters for the two ports of the lens antenna. The results indicate a significant bandwidth of up to 46.3% (7.8–13.8 GHz), with reflection coefficients consistently below –10 dB. Furthermore, the isolation between the two ports exceeds 29 dB.

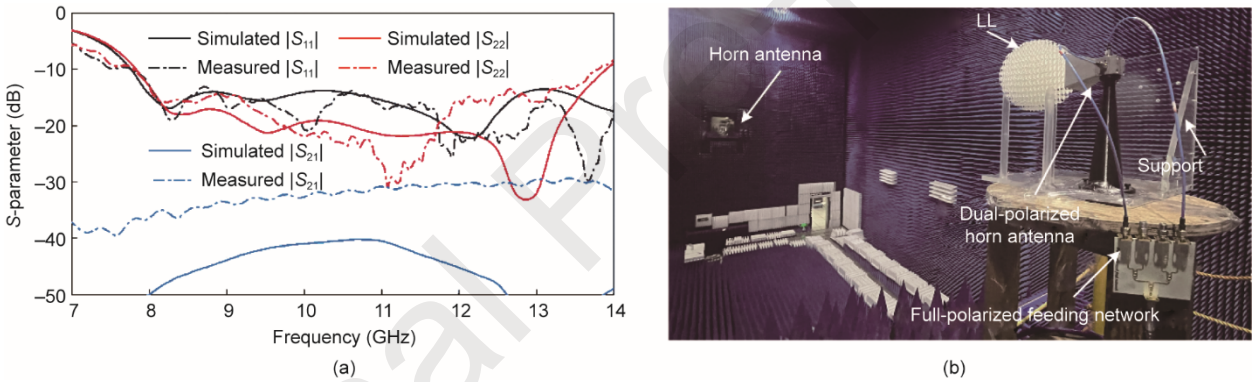


**Fig. 9.** (a) Simulated and measured *S*-parameters of the proposed LL with a single feed; (b) experimental setup for the proposed LL antenna system in an anechoic far-field chamber.

The feeding network introduced in Section 3 was utilized to produce distinct excitations for the dual-polarized horn, enabling the achievement of feeding sources with different polarizations. The radiation performance of the feeding source in different radiation states was tested in an anechoic far-field chamber, as shown in Fig. 9(b). The simulated and measured normalized radiation patterns of the entire LL antenna for six polarizations at three frequencies (i.e., 8, 10, and 12 GHz) are plotted in Fig. 10. The simulated and measured gains for the six polarizations of the proposed LL antenna, along with axial ratios (ARs) for circular polarization (CP), are shown in Fig. 11(a). It should be noted that the insertion loss induced by the coaxial cable adapter and power divider network was meticulously calibrated. For the linear polarization (LP), the measured gains fluctuate between 16.7 and 20.3 dB across the operating band, ranging from 7.8 to 12.7 GHz. In the case of theCP, the slight deficiencies in the fabrication process of the sextuple polarization feeding network and the horn antenna, as well as measurement errors such as misalignment, and so forth, lead to the degradation of the AR within the 8–12 GHz spectrum.

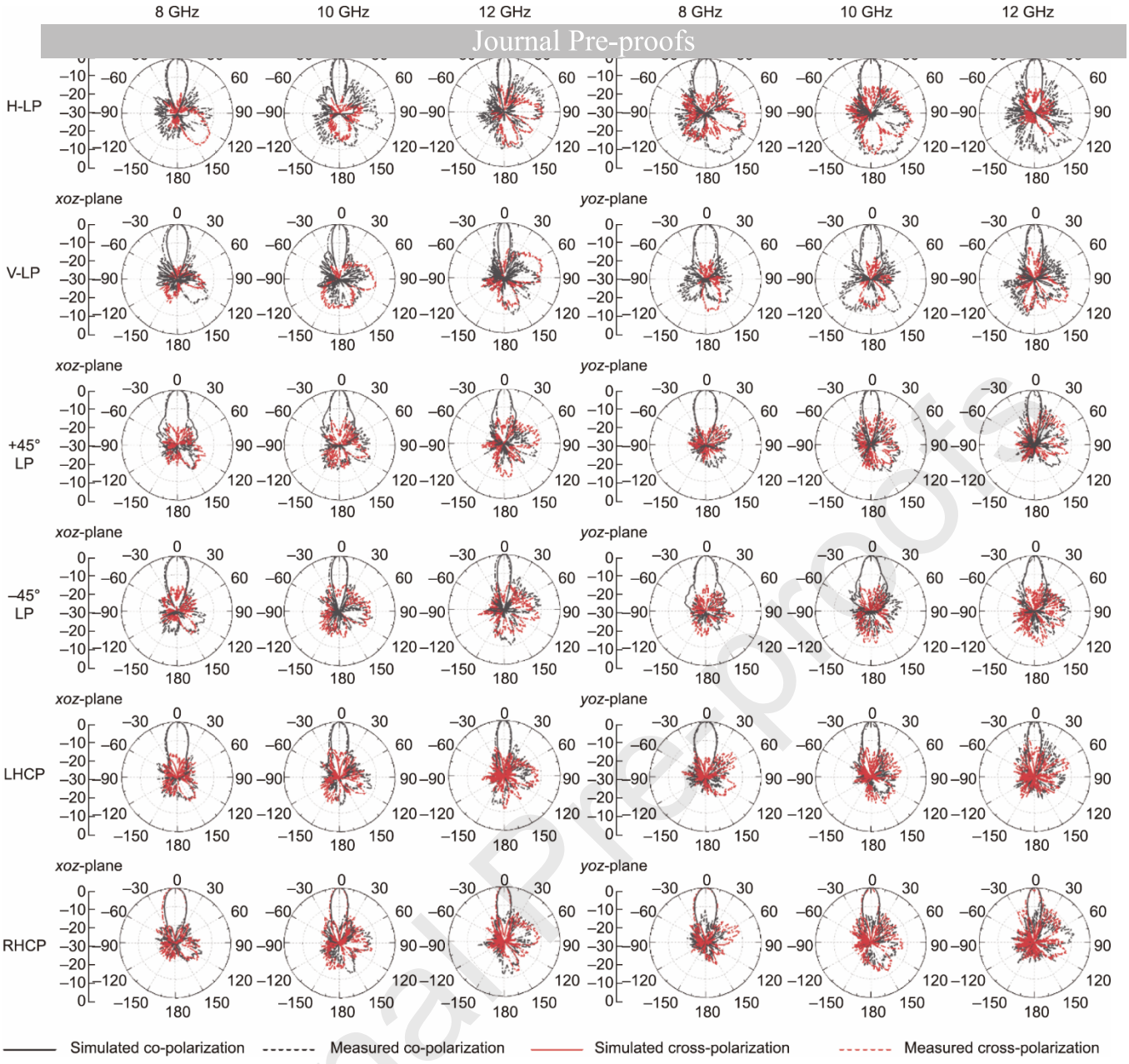


**Fig. 10.** Simulated and measured normalized radiation patterns of the LL antenna.

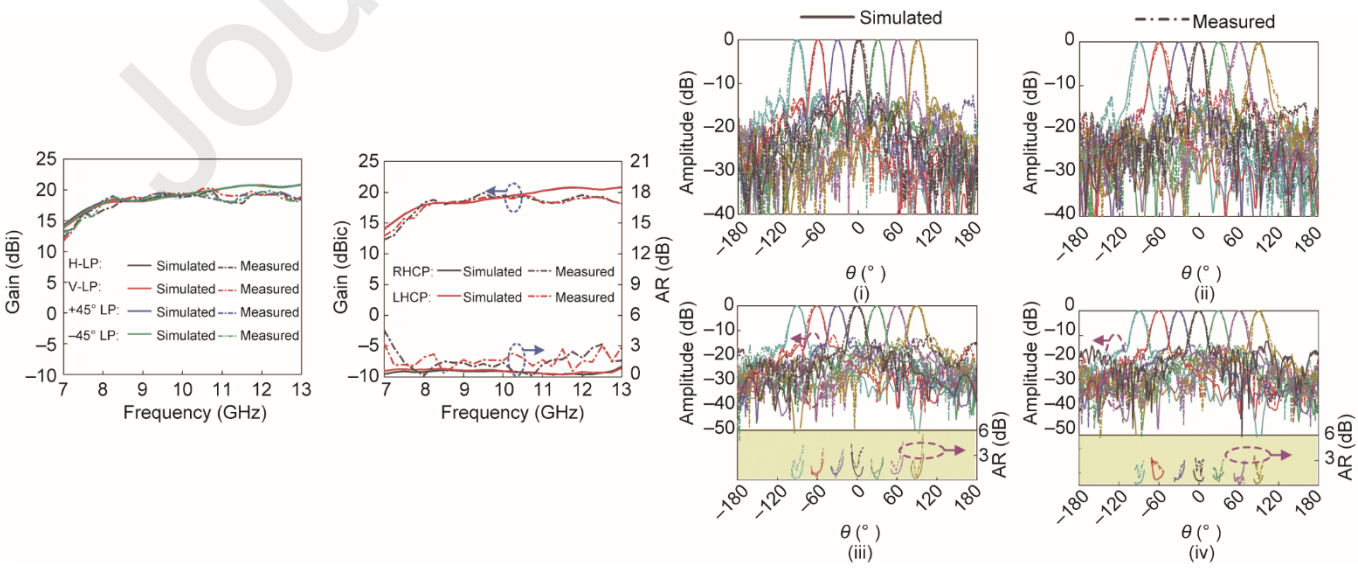

**Fig. 11.** (a) Simulated and measured gains for (i) LP and (ii) CP. (b) Simulated and measured normalized scanning patterns of the proposed lens at 10



Upon a comprehensive review, it was found that various factors—such as fabrication errors, limitations in the dynamic range of the testing equipment, excitation imbalances, and environmental influences—had collectively contributed to a slight degradation in the obtained results. Nevertheless, the measured results convincingly demonstrate the insensitivity of the gain to polarization variations, thereby confirming the isotropy of the proposed LL antenna design. Fig. 11(b) presents the simulated and measured normalized scanning patterns of the proposed lens antenna at 10 GHz for various polarizations (i.e., H-LP, V-LP, LHCP, and RHCP) in the *xoz*-plane. By rotating the horn antenna to arbitrary angles, the innovative LL antenna can seamlessly achieve a scanning range of 360° in the azimuth plane and ±90° in the elevation plane.

## 5. Discussion

In order to showcase the merits of the proposed lightweight LL antenna, we have devised a comparative study with a conventional LL antenna constructed using cubic lattices with an identical radius, as shown in Figs. 12(a) and (b), which was demonstrated to exhibit near isotropy in Ref. [26]. The design and placement of the feeding horn antenna are consistent with our previous settings. Fig. 12(c) compares the normalized radiation patterns in different polarizations (i.e., H-LP and V-LP) between the two LLs. The normalized radiation patterns of both the traditional LL and our design at 10 GHz exhibit remarkable similarities in terms of cross-polarization discriminations. However, the simulated sidelobe level of our design is more than –14 dB in both the E-plane and H-plane, whereas that of the traditional conventional LL only reaches –10.2 dB. This phenomenon stems from the fact that the spatially varying permittivity distributions in different lens structures create distinct electromagnetic wave propagation paths through differential refraction and reflection, leading to characteristic phase/amplitude modulations that produce different far-field interference patterns and radiation characteristics. The commercial software SolidWorks was employed to analyze the weight, and the results revealed that the proposed lens weighs only 55.8% of the mass of the conventional LL—clearly demonstrating the outstanding weight-saving performance achieved through the utilization of a diamond lattice structure.

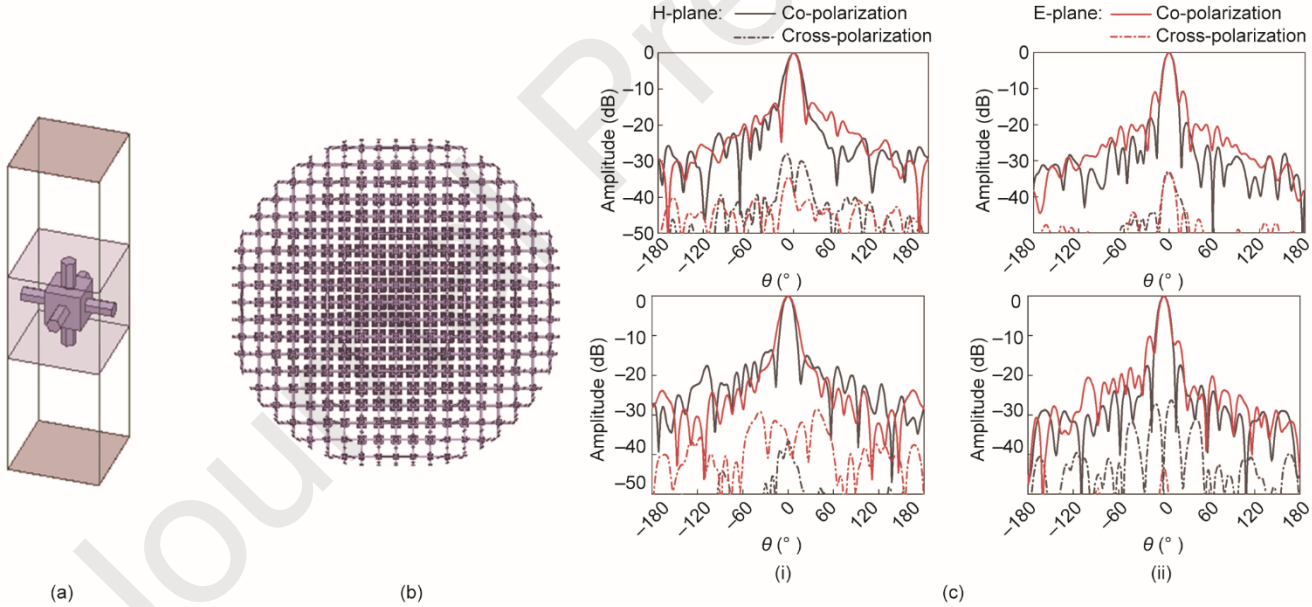


**Fig. 12.** Traditional LL structure: (a) cubic lattice cell and (b) front view. (c) Comparison of normalized radiation patterns between (i) the proposed LL antenna constructed using a diamond lattice structure: H-LP (top) and V-LP (bottom) and (ii) a traditional LL antenna constructed using a cubic lattice structure: H-LP (top) and V-LP (bottom).

Table 4 [5,11,12,14,18,19,22,25–28,30,35,41–44] showcases a performance comparison between the proposed antenna design and several previously reported representative LL antennas. When compared with spherical LLs [5,22,25–28,30,35], cylindrical configurations [14,43], parallel-plate waveguide/dielectric slab configurations [18,19,42,44], PCB-based implementations [11,12], and especially specialized configurations such as the semi-compressed elliptical LL in Ref. [41] significantly undermine the 2D multibeam capability, even though they offer reduced profiles. Hence, full-scale lenses have irreplaceable advantages. In the design of spherical lenses, a diverse range of unit structures have been adopted. However, some of these structures are based on asymmetric cell designs, such as slabs [27], rings [28], and posts [26,30], which prevents them from achieving full-angle scanning in both the elevation and azimuth planes. As a result, some of these structures have been repurposed for polarization conversion applications [27,30]. An innovative radial conical hole-type lens introduced in Ref. [5] is capable of collecting electromagnetic waves across various incidence angles and polarizations. Nevertheless, it operates within a notably limited bandwidth. Similarly, the lenses presented in Ref. [22] have a relatively large physical size, extending up to $5.12\lambda_0$ (where $\lambda_0$ is defined as the wavelength in free space at central frequency). The lens design in Ref. [35], which is based on a BCC lattice configuration, requires the insertion of conductive

cubes into foam support structures, leading to significant manufacturing complexity. In comparison, our design not only retains the advantages of convrized radiation while featuring a remarkably lightweight, environmentally friendly and fabrication-simplified architecture. In addition, this work presents an innovative design methodology that harnesses crystallographic principles to design and optimize electromagnetic components. Design goals can be achieved through a multidimensional strategy that seamlessly integrates considerations of structural design, material properties, and wave manipulation. This approach provides invaluable insights for propelling the development of wireless communication technologies and serves as a catalyst for fostering the synergistic connection between the fields of materials science and electromagnetic engineering.

**Table 4**

Comparison of our proposed LL with recently reported LLs.

| Ref. | Shape | Size ($\lambda_0 \times \lambda_0 \times \lambda_0$) | Realization | Polarization | Frequency (GHz) | Operating bandwidth[a] | Gain (dBi/dBic) | Scanning range[b] |
|---|---|---|---|---|---|---|---|---|
| [5] | Sphere | 2.6 × 2.6 × 2.6 | 3DP (radial conical hole) | CP | 7.9 | > 6.3% | 14.3–15.3 | 2D: ±90° and 360° |
| [11] | Dielectric substrates | 9.7 × 5.2 × 0.025 | PCB with air holes | LP | 9.25 | 27% | ~11–15.3 | 2D: 82° and 97° |
| [12] | Dielectric substrates | 14 × 14 × 0.12 | PCB with crossed sinusoidal-shaped transmission lines | LP | 260 | 25% | ~23.75 | 1D: 360° |
| [14] | Cylinder | 3.6 × 3.6 × 0.4 | 3DP (holes) | LP | 15 | ＞40% | 16.5–19.1 | 2D: ±20° and ±20° (3dB loss) |
| [18] | Parallel plate | 13 × 13 × 1.5 | CNC machine (hexagonal posts) | LP | 28.7 | 26.1% | ~25–28 | 2D: 100° and 100° |
| [19] | Parallel plate | 10 × 10 × 0.16 | CNC machine (geodesic) | LP | 62 | 16.1% | 19–21 | 1D: 360° |
| [22] | Sphere | 5.1 × 5.1 × 5.1 | 3DP (icosahedron) | Dual-CP | 31.75 | 33.1% | 19–21.2 | 2D: ±90° and 360° |
| [25] | Sphere | 4 × 4 × 4 | 3DP (cube lattice) | LP | 10 | ＞40% | 17.3–20.8 | 2D: ±90° and 360° |
| [26] | Sphere | 3.7 × 3.7 × 3.7 | 3DP (posts and cubes) | Dual-LP | 33 | ＞40% | 17.2–21.3 | 2D: ±60° and360° |
| [27] | Sphere | 3 × 3 × 3 | 3DP (slab) | LP to CP | 10 | ＞40% | 16–18.6 | 1D: 360° |
| [28] | Sphere | 5.3 × 5.3 × 5.3 | 3DP (rings) | LP | 33 | 40% | 18.6–21.2 | 2D: ±70° and360° |
| [30] | Sphere | 3.5 × 3.5 × 3.5 | 3DP (posts) | Dual LP to CP | 30 | 23% | 17.8–19.2 | 1D: 360° |
| [35] | Sphere | 4.7 × 4.7 × 4.6 | Additive manufacturing (conductive BCC | Dual-LP | 3.55 | 14.1% | 21.2–23.3 | 2D: ±90° and360° |

| | | | | | | | | |
|---|---|---|---|---|---|---|---|---|
| | | | in cubic grid) | | | | | |
| [41] | Half-compressed ellipse | 6.5 × 6.5 × 5.1 | 3DP (cube lattice) | LP | 110 | Single frequency | 21.3 | 1D: ±52° (3 dB loss) |
| [42] | Parallel plate | 6 × 6 × 0.33 | CNC machine (inserted all-metal cube) | LP | 10 | 40% | 15.8–21 | 1D: 360° |
| [43] | Cylinder | 4.2 × 4.2 × 2.4 | 3DP (posts and slabs) | LP to CP | 35 | 11.4% | 13.1–15 | 1D: 360° |
| [44] | Half parallel plate | 9 × 4.5 × 0.18 | 3DP (glide symmetric structure) | LP | 27 | 37% | ~14–18.5 | 1D: 50° |
| This work | Sphere | 4.6 × 4.6 × 4.6 | 3DP (diamond lattice) | Dual-LP Dual-CP ±45° LP | 10 | ＞40% | 16.7–20.3 | 2D: ±90° and 360° |

$\lambda_0$ is defined as the wavelength in free space at central frequency.

[a] The operating bandwidth of the LP LL antenna is defined as the –10 dB impedance bandwidth, while that of the circularly polarized LL antenna is the overlap of the –10 dB impedance and 3 dB AR bandwidth.

[b] The coverage achieved by a single feed illuminating the lens.

## 6. Conclusions

This article demonstrates a lightweight, fabrication-simplified, full-polarized LL antenna that boasts a wide bandwidth, high gain, and lower sidelobe levels. The diamond lattice structure introduced in the LL design increases the robustness of the antenna against incident angles while simultaneously reducing its overall weight. By leveraging 3DP technology, a sophisticated structure was brought to fruition. The integration of a meticulously designed dual-polarized horn antenna, in conjunction with a sextuple-polarized broadband feeding network as the source, validates the ability of the LL to exhibit consistent isotropic radiation potential characteristics across the entire X-band. These distinctive features not only position the proposed LL antenna as a promising technology for integrated communication, sensing, and transmission applications but also provide valuable insights for the ongoing convergence of materials science and electromagnetic engineering.


## Acknowledgments

This work was supported by the National Science Foundation of China (62301152 and 62188102), the Fundamental Research Funds for the Central Universities (2242022k60003), and the Youth Talent Promotion Foundation of Jiangsu Science and Technology Association (TJ-2023-074).


## References


[1] Hong W, Jiang ZH, Yu C, Zhou J, Chen P, Yu Z, et al. Multibeam antenna technologies for 5G wireless communications. IEEE Trans Antennas Propag 2017;65(12):6231–49.

[2] Vázquez MÁ, Perez-Neira A, Christopoulos D, Chatzinotas S, Ottersten B, Arapoglou PD, et al. Precoding in multibeam satellite communications: present and future challenges. IEEE Wirel Commun 2016;23(6):88–95.

[3] Lin Q, Xu J, Chen K, Wang L, Li W, Yu Z, et al. A single-board integrated millimeter-wave asymmetric full-digital beamforming array for B5G/6G applications. Engineering 2024;41:35–50.

[4] Chen K, Xu J, Zhao R, Xiang L, Hou D, Yu Z, et al. Compact millimeter-wave, dual-band, dual-polarized, and duplex-scalable phased array enabling B5G/6G multistandard systems. Engineering 2025. In press.

[5] Liu K, Zhao C, Qu SW, Chen Y, Hu J, Yang S. A 3-D-printed multibeam spherical lens antenna with ultrawide-angle coverage. IEEE Antennas Wirel Propag Lett 2021;20(3):411–5.

[6] Luneburg RK. Mathematical theory of optics. California: University of California Press; 1966.

[7] Savanskiy A, Glybovski S, Akimov VP, Filonov D, Belov P, Meshkovskiy I. Broadband 3-D Luneburg lenses based on metamaterials of radially d

[8] Boriskin AV, Vorobyov A, Sauleau R. Two-shell radially symmetric dielectric lenses as low-cost analogs of the Luneburg lens. IEEE Trans Antennas Propag 2011;59(8):3089–93.

[9] Bor J, Lafond O, Merlet H, Le Bars P, Himdi M. Technological process to control the foam dielectric constant application to microwave components and antennas. IEEE Trans Compon Packaging Manuf Technol 2014;4(5):938–42.

[10] Mateo-Segura C, Dyke A, Dyke H, Haq S, Hao Y. Flat Luneburg lens via transformation optics for directive antenna applications. IEEE Trans Antennas Propag 2014;62(4):1945–53.

[11] Lei S, Wei G, Han K, Qiu T, Wang M. 2-D multibeam leaky-wave antenna based on modified Luneburg lens. IEEE Antennas Wirel Propag Lett 2024;23(5):1453–7.

[12] Mahmoud A, Ruiz-García J, de Sagazan O, Ettorre M, Sauleau R, González-Ovejero D. Low-cost and low-profile sub-terahertz Luneburg lens beamformer on polymer. IEEE Antennas Wirel Propag Lett 2023;22(6):1411–5.

[13] Ströber T, Lassauce L, Morvan X, Legay H, Goussetis G, Ettorre M. Wide-angle scanning parallel-plate lens in multilayer PCB technology. IEEE Trans Antennas Propag 2024;72(10):7436–47.

[14] Lou YH, Zhu YX, Fan GF, Lei W, Lu WZ, Wang XC. Design of Ku-band flat Luneburg lens using ceramic 3-D printing. IEEE Antennas Wirel Propag Lett 2021;20(2):234–8.

[15] Chen K, Xu J, Lin Q, Zhu Y, Hong W. Single-layer wideband tilted beam phased array antenna for millimeter-wave vehicle communications. IEEE Trans Veh Technol 2024;73(3):3536–50.

[16] Zheng YX, Xiang BJ, Pan YM, Zheng SY. Compact cylinder Luneburg-lens antennas based on 3-D-printing technology. IEEE Trans Antennas Propag 2023;71(3):2311–20.

[17] Castillo-Tapia P, Yang S, Palomares-Caballero Á, Guillet JP, Fonseca NJG, Quevedo-Teruel O. Sub-THz fully-metallic geodesic Luneburg lens antenna. IEEE Trans Terahertz Sci Technol 2025;15(3):514–8.

[18] Bilitos C, Morvan X, Sauleau R, Martini E, Maci S, González-Ovejero D. Series dual-fed continuous transverse stub array with enhanced multibeam operation enabled by a reflective Luneburg lens. IEEE Trans Antennas Propag 2024;72(11):8420–32.

[19] Zetterstrom O, Arnberg P, Vidarsson FV, Algaba-Brazález A, Manholm L, Johansson M, et al. V-band geodesic generalized Luneburg lens antenna with high beam crossover gain. IEEE Trans Antennas Propag 2023;71(9):7591–6.

[20] Mittra R, Nasri A, Arya RK. Wide-angle scanning antennas for millimeter-wave 5G applications. Engineering 2022;11:60–71.

[21] Zhao LW, Wu YF, Wang C, Guo Y. A 3-D-printed deployable Luneburg lens antenna based on the pop-up kirigami sphere. IEEE Trans Antennas Propag 2023;71(8):6481–9.

[22] Wang C, Wu J, Guo YXA. 3-D-printed multibeam dual circularly polarized Luneburg lens antenna based on quasi-icosahedron models for Ka-band wireless applications. IEEE Trans Antennas Propag 2020;68(8):5807–15.

[23] Feng PY, Qu SW, Yang S. Defocused cylindrical Luneburg lens antennas with phased array antenna feed. IEEE Trans Antennas Propag 2019;67(9):6008–16.

[24] Marin JG, Hesselbarth J. Lens antenna with planar focal surface for wide-angle beam-steering application. IEEE Trans Antennas Propag 2019;67(4):2757–62.

[25] Liang M, Ng WR, Chang K, Gbele K, Gehm ME, Xin H. A 3-D Luneburg lens antenna fabricated by polymer jetting rapid prototype. IEEE Trans Antennas Propag 2014;62(4):1799–807.

[26] Guo Y, Li Y, Wang J, Ge L, Zhang Z, Chen M, et al. A 3D printed nearly isotropic Luneburg lens antenna for millimeter-wave vehicular networks. IEEE Trans Veh Technol 2022;71(2):1145–55.

[27] Lei S, Han K, Li X, Wei G. A design of broadband 3-D-printed circularly polarized spherical Luneburg lens antenna for X-band. IEEE Antennas Wirel Propag Lett 2021;20(4):528–32.

[28] Li Y, Ge L, Chen M, Zhang Z, Li Z, Wang J. Multibeam 3-D-printed Luneburg lens fed by magnetoelectric dipole antennas for millimeter-wave MIMO applications. IEEE Trans Antennas Propag 2019;67(5):2923–33.

[29] Wang C, Wu J, Guo YXA. 3-D-printed wideband circularly polarized parallel-plate Luneburg lens antenna. IEEE Trans Antennas Propag 2020;68(6):4944–9.

[30] Wang Z, Tan Q, Yang D, Fan K, Yu W, Liu L, et al. A wideband dual circularly polarized Luneburg lens multibeam antenna feed by dual linearly polarized ME-dipole antennas. IEEE Trans Antennas Propag 2025;73(5):2804–13.

[31] Larimore Z, Jensen S, Good A, Lu A, Suarez J, Mirotznik M. Additive manufacturing of Luneburg lens antennas using space-filling curves and fused filament fabrication. IEEE Trans Antennas Propag 2018;66(6):2818–27.

[32] Kittel C. Introduction to solid state physics. Hoboken: Wiley; 2004.



[33] Smith DR, Schultz S, Markoš P, Soukoulis CM. Determination of effective permittivity and permeability of metamaterials from reflection and transmission coefficients. Phys Rev B Condens Matter 2002;65(19):195104.

[34] Hasar UC, Westgate CR. A broadband and stable method for unique complex permittivity determination of low-loss materials. IEEE Trans Microw Theory Tech 2009;57(2):471–7.

[35] Ansari M, Zetterstrom O, Fonseca NJG, Quevedo-Teruel O, Guo YJ. A lightweight spherical generalized Luneburg lens antenna with low cross-polarization over a wide range in azimuth and elevation. IEEE Open J Antennas Propag 2024;5(1):58–66.

[36] Oktafiani F, Hamid EY, Munir A. Wideband dual-polarized 3D printed quad-ridged horn antenna. IEEE Access 2022;10:8036–48.

[37] Park JS, Wang H. A fully differential ultra-compact broadband transformer-based Wilkinson power divider. IEEE Microw Wirel Compon Lett 2016;26(4):255–7.

[38] Oraizi H, Sharifi AR. Design and optimization of broadband asymmetrical multisection Wilkinson power divider. IEEE Trans Microw Theory Tech 2006;54(5):2220–31.

[39] Zheng SY, Chan WS, Man KF. Broadband phase shifter using loaded transmission line. IEEE Microw Wirel Compon Lett 2010;20(9):498–500.

[40] Pozar DM. Microwave engineering. Hoboken: Wiley; 2005.

[41] Meng F, Guo Y, Ma K, Luo Y. A terahertz wide-angle beamsteering 3-D printed half-compressed elliptical Luneburg lens with planar focal plane. IEEE Antennas Wirel Propag Lett 2024;23(2):843–7.

[42] Lian JW, Ansari M, Hu P, Guo YJ, Ding D. Wideband and high-efficiency parallel-plate Luneburg lens employing all-metal metamaterial for multibeam antenna applications. IEEE Trans Antennas Propag 2023;71(4):3193–203.

[43] Zheng YX, Xiang BJ, Pan YM, Zheng SY. Compact cylinder Luneburg-lens antennas based on 3-D-printing technology. IEEE Trans Antennas Propag 2023;71(3):2311–20.

[44] Zetterstrom O, Fonseca NJG, Quevedo-Teruel O. Compact half-Luneburg lens antenna based on a glide-symmetric dielectric structure. IEEE Antennas Wirel Propag Lett 2022;21(11):2283–7.



## Declaration of Interest Statement

☒ The authors declare that they have no known competing financial interests or personal relationships that could have appeared to influence the work reported in this paper.

☐ The author is an Editorial Board Member/Editor-in-Chief/Associate Editor/Guest Editor for this journal and was not involved in the editorial review or the decision to publish this article.

☐ The authors declare the following financial interests/personal relationships which may be considered as potential competing interests: